# Energy & Environmental Science



### **PAPER**

View Article Online
View Journal



Cite this: DOI: 10.1039/d2ee01844f

# Machine learning-assisted ultrafast flash sintering of high-performance and flexible silver—selenide thermoelectric devices†

Flexible thermoelectric generators (TEGs) have shown immense potential for serving as a power source for wearable electronics and the Internet of Things. A key challenge preventing large-scale application of TEGs lies in the lack of a high-throughput processing method, which can sinter thermoelectric (TE) materials rapidly while maintaining their high thermoelectric properties. Herein, we integrate highthroughput experimentation and Bayesian optimization (BO) to accelerate the discovery of the optimum sintering conditions of silver-selenide TE films using an ultrafast intense pulsed light (flash) sintering technique. Due to the nature of the high-dimensional optimization problem of flash sintering processes, a Gaussian process regression (GPR) machine learning model is established to rapidly recommend the optimum flash sintering variables based on Bayesian expected improvement. For the first time, an ultrahigh-power factor flexible TE film (a power factor of 2205  $\mu$ W m<sup>-1</sup> K<sup>-2</sup> with a zT of 1.1 at 300 K) is demonstrated with a sintering time less than 1.0 second, which is several orders of magnitude shorter than that of conventional thermal sintering techniques. The films also show excellent flexibility with 92% retention of the power factor (PF) after 10<sup>3</sup> bending cycles with a 5 mm bending radius. In addition, a wearable thermoelectric generator based on the flash-sintered films generates a very competitive power density of 0.5 mW cm<sup>-2</sup> at a temperature difference of 10 K. This work not only shows the tremendous potential of high-performance and flexible silver-selenide TEGs but also demonstrates a machine learning-assisted flash sintering strategy that could be used for ultrafast, high-throughput and scalable processing of functional materials for a broad range of energy and electronic applications.

Received 9th June 2022, Accepted 27th September 2022

DOI: 10.1039/d2ee01844f

rsc.li/ees

#### **Broader context**

Thermoelectric devices offer great opportunities in direct conversion of waste heat into electricity and solid-state refrigeration with no moving parts or environmental emission from refrigerants. To realize their broad applications in energy harvesting and cooling, significant advances are required to not only increase the thermoelectric figure of merit zT but also improve the mechanical flexibility and reduce the manufacturing time and cost. Although nanoscale materials offer opportunities to enhance zT by tailoring the electron and phonon transport, challenges still remain in processing these nanoscale materials into high-performance and low-cost devices. Here, we demonstrate a machine learning-assisted high-throughput and ultrafast (<1 second) photonic flash processing method that sinters silver–selenide nanoparticles into flexible films with room temperature zT > 1, which is among the highest in flexible thermoelectric materials. Bayesian optimization was applied to accelerate the discovery of the optimum sintering conditions using less than 40 experiments, despite the complexity of photonic flash sintering processes. The successful integration of high-throughput photonic flash processing and machine learning can be generalized to highly scalable and low-cost manufacturing of a broad range of energy and electronic materials.

# 1. Introduction

Flexible thermoelectric generators (TEGs) are promising candidates for developing self-powered wearable devices and industrial Internet of Things. <sup>1–5</sup> Flexible TEGs are light weight, compact, and maintenance-free solid-state energy convertors with no moving parts that directly convert heat into electricity, and they can easily conform to a variety of heat sources with

<sup>&</sup>lt;sup>a</sup> Department of Aerospace and Mechanical Engineering, University of Notre Dame, Notre Dame, IN 46556, USA. E-mail: yzhang45@nd.edu

b Department of Chemical and Biomolecular Engineering, University of Notre Dame, Notre Dame, IN 46556, USA

<sup>&</sup>lt;sup>c</sup> Department of Mechanical and Aerospace Engineering, California State University Long Beach, Long Beach, CA 90840, USA

<sup>&</sup>lt;sup>d</sup> Department of Chemical Engineering, Texas Tech University, Lubbock, TX 79409,

<sup>†</sup> Electronic supplementary information (ESI) available. See DOI: https://doi.org/10.1039/d2ee01844f

curved surfaces (e.g., body heat). The efficiency of thermoelectric (TE) materials largely depends on the dimensionless figure of merit (zT) defined as  $zT = \frac{\sigma S^2}{\kappa}T$ , where S,  $\sigma$ ,  $\kappa$ , and T denote the Seebeck coefficient, electrical conductivity, thermal conductivity, and absolute temperature, respectively. 6-8 Despite the significant progress achieved in thermoelectric materials to date, Bi<sub>2</sub>Te<sub>3</sub>-based alloys remain as dominant materials for thermoelectric applications near room temperature, and the zTfor n-type TE materials still remains below or around unity at room temperature. 6,9,10 In addition, the scarcity of tellurium (Te) necessitates the development of new tellurium-free thermoelectric materials for use in widespread industrial and wearable applications. Silver-selenide (Ag<sub>2</sub>Se) is a narrow-band gap n-type chalcogenide and an ideal candidate for room-temperature applications owing to its high power factor (PF) and low intrinsic thermal conductivity. 11-20

Sintering is an essential step in material processing to improve transport properties. Sintering transforms TE particles into a dense structure with improved thermoelectric properties. Conventional thermal sintering requires hours of processing time at elevated temperatures, which hinders the widespread development of flexible TEGs on organic substrates of a low melting point (e.g., polymers and fabrics). In addition, it hampers the high-throughput discovery and energy-efficient manufacturing of high-performance TE materials with optimized compositions. Substantial effort has been devoted to the development of innovative sintering methods, such as microwave-assisted sintering, spark plasma sintering (SPS), chemical sintering, and intense pulsed light (flash) sintering.21-29 Among these techniques, flash sintering using intense pulsed light is uniquely advantageous. For example, it is ultrafast, energy-efficient, and can sinter the TE films at elevated temperatures on low-melting point substrates without damaging the underneath substrate. Although flash sintering has been used for a variety of conductive materials such as silver, copper, and graphene, it remains relatively underexplored for semiconducting nanomaterials, particularly TE materials. 28-32 Sintering of TE nanoparticles constitutes a complex process involving solvent evaporation, decomposition of organic ingredients, formation of inter-particle conduction pathways, and densification, which highlights the imperative role of optimized flash sintering variables in the resulting TE properties.

Previous efforts to discover the optimum flash sintering variables relied on expert-driven Edisonian trial-and-error search, which is time- and labor-intensive.<sup>32</sup> Enabled by recent advances in machine learning, data-driven approaches such as Bayesian optimization (BO) have rapidly permeated many fields including TE materials, 33-35 smart manufacturing, 36-38 and molecular modeling of chemical products.<sup>39,40</sup> Novel artificial intelligence (AI) systems enable automated prediction and optimization of materials and additive manufacturing processes. 33,36-38 Moreover, machine learning algorithms can help to both intelligently maximize specific performance metrics and aid in revealing the underlying physical mechanisms. Although classical statistical design of experiments (e.g., full/partial factor design, response surface methods, and ANOVA analysis) has been used to improve

TE materials and manufacturing, 41-43 these approaches require experimental designs to be fixed at the beginning of an optimization iteration and the experimental design cannot be updated as new data become available during the optimization iteration. This is inefficient and requires many experiments to optimize multiple factors simultaneously. BO overcomes these limitations by adaptively determining a sequence of experiments without assuming a parametric model for the data. In BO, the non-parametric GPR model is updated after each experiment is completed such that decisions are made based on all of the available data. For this reason, BO is replacing response surface design of experimental methods as the state-of-the-art for statistical optimization of laboratory experiments. 44,45

Despite the renewed interest and recent success of AI and machine learning, there are often significant barriers in translating these methods into new application domains. In this work, we integrate, for the first time, flash sintering with a Gaussian process regression (GPR) machine learning model and BO to predict the optimum flash sintering variables for n-type silver-selenide TE films that leads to maximum PF at room temperature. The proposed methodology successfully optimized four sintering variables - voltage, pulse duration, number of pulses, and pulse delay time - resulting in a PF of 2205  $\mu$ W m<sup>-1</sup> K<sup>-2</sup> and a corresponding zT of 1.1 at room temperature (among the highest in the reported flexible TE films) with a sintering time less than 1.0 second after only 32 experiment-machine learning iterations. This methodology could be easily generalized to ultrafast and high-throughput flash sintering of a diverse range of energy and electronic materials and other manufacturing processes in general.

# 2. Results and discussion

Fig. 1 depicts our machine learning-assisted workflow to find the optimum flash sintering variables for silver-selenide TE films fabricated using vacuum-assisted filtration technique. The aim of this framework is to find a set of variables including voltage, pulse duration, the number of pulses, and pulse delay that yield the maximum power factor with a minimum number of experimental iterations. The workflow starts with flash sintering of silver-selenide films and then measuring the power factor of the films (Fig. 1). The sintering variables and measured power factor are then used as an input for BO to predict the next set of variables to test.

The preparation of silver-selenide nanostructures was based on the process reported in previous studies. 11,20 Details of the synthesis are provided in the Materials and methods section and Fig. S1 (ESI†). The as-prepared products were dispersed in ethanol by sonication and then deposited on a flexible porous filtration membrane with an average pore diameter of 0.22 µm (Tisch Scientific) by vacuum filtration. The as-prepared films were dried in a vacuum and then cold-pressed at 25 MPa for 15 min prior to flash sintering (Fig. S2, ESI†). During the fabrication process, the film thicknesses were controlled by varying the silver-selenide particle concentration (Fig. S3, ESI†).

# ( i ) Intense pulsed light (flash) sintering

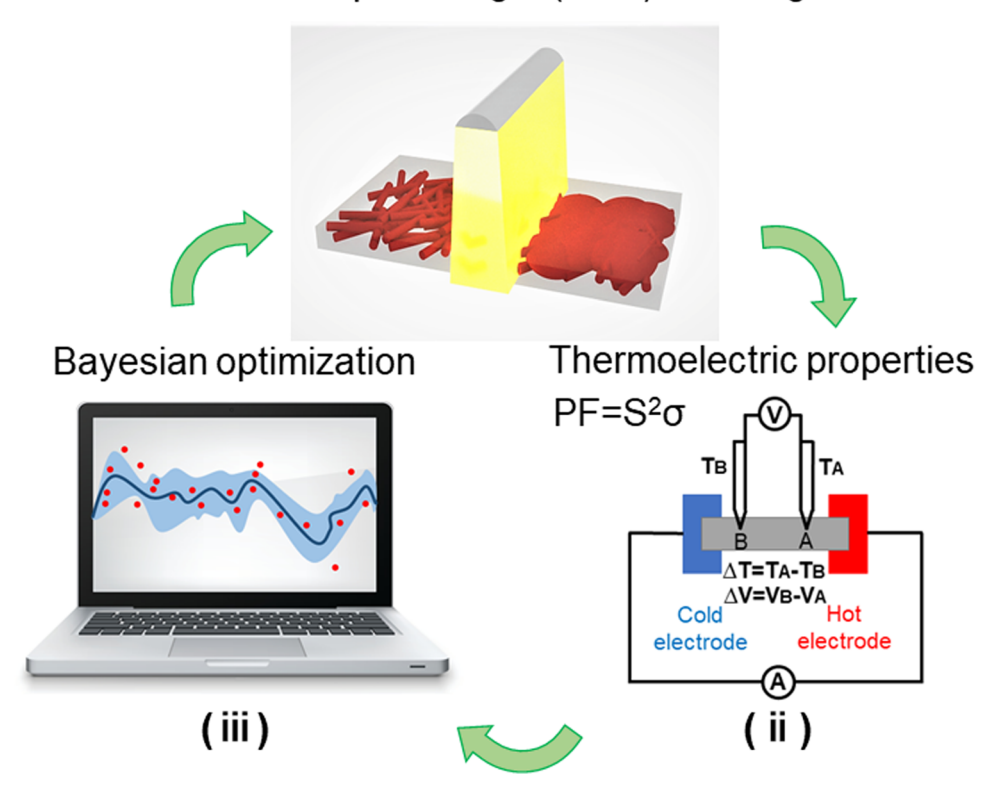


Fig. 1 Schematic workflow of the machine learning-assisted flash sintering of silver-selenide TE films. (i) Intense pulsed light (flash) sintering. (ii) Thermoelectric property measurement of the sintered film including the electrical conductivity and the Seebeck coefficient. (iii) Bayesian optimization algorithm for the evaluation and suggestion of new sintering variables (voltage, pulse duration, number of pulses, and pulse delay) to test.

The structure and phase composition of the as-prepared silver-selenide powder was characterized by X-ray diffraction (XRD). Fig. S4(a) (ESI†) displays the XRD pattern of the synthesized silver-selenide nanostructures before flash sintering. All the peaks in the pattern can be indexed to orthorhombic silver-selenide (JCPDF 24-1041), indicating that there are no obvious impurities. Fig. S4(b) and (c) (ESI†) shows the surface SEM images of the fabricated film before sintering, exhibiting a porous microstructure with randomly distributed silver-selenide nanostructures with diameters in the range of 50–200 nm.

Fig. 2 shows the TE properties and microstructure of the films under different sintering conditions listed in Table S1 (ESI†). Details of the TE property measurement process are described in the Materials and methods section. Overall, 37 experiments with a unique set of sintering variables were tested, and three films were sintered under each condition to ensure the reproducibility of the results. The SEM-EDS map of the element distribution of unsintered silver-selenide films confirms the Ag/Se molar ratio of 1.9:1 (see Fig. S5 and Table S2, ESI†). A previous study has shown that adding a small excess of anions (Se) to the stoichiometric composition leads to a significant increase in the power factor over stoichiometric Ag<sub>2</sub>Se.<sup>47</sup> This extra Se significantly enhances carrier mobility and inhibits the formation of the metastable structure. Thus, we synthesized silver-selenide nanostructures with  $\sim 5\%$  excess of selenium (Ag<sub>1.9</sub>Se) to maximize the power factor. The silver-selenide films were fabricated with eight different thicknesses (16.5  $\mu$ m, 14.3  $\mu$ m, 13.3  $\mu$ m, 9.0  $\mu$ m, 3.8  $\mu$ m, 2.7  $\mu$ m, 2.4  $\mu$ m, and 2.3  $\mu$ m) and were classified into two general groups. Experiments 1–22 and 23–37 were conducted with films with average general thicknesses of 12.5  $\pm$  3.2  $\mu$ m and 2.6  $\pm$  0.5  $\mu$ m, respectively (Table S1, ESI†).

The typical light emission from the flash lamp (xenon, type C) is within 200–700 nm. Room-temperature in-plane TE properties of the sintered films are shown in Fig. 2(a) and (b). Sintered films under the BO-optimized variables in experiment 32 (2.3 kV, 1.5 ms pulse time, 4 pulses, and 293 ms pulse delay) led to a Seebeck coefficient and an electrical conductivity of  $-161.7~\mu V~K^{-1}$  and  $8.4\times10^4~S~m^{-1}$ , respectively, with a maximum PF of 2205  $\pm$  73.1  $\mu W~m^{-1}~K^{-2}$  at room temperature, which is among the highest in the reported flexible TE films and comparable to that of the bulk Ag<sub>2</sub>Se.  $^{16,48-50}$  It is worth noting that the total sintering time was less than a second whereas conventional thermal sintering usually takes 30 min or more (Table 1).

Fig. 2(c)–(e) demonstrates the surface SEM images of unsintered films and flash-sintered films with representative non-optimum (experiment 24) and optimum (experiment 32) variables. As shown in Fig. 2(c), unsintered silver–selenide nanostructures are randomly distributed with a porous microstructure and limited carrier mobility, which result in a very low PF of 101.3  $\mu$ W m<sup>-1</sup> K<sup>-2</sup>. A single pulse with a deposition energy of  $\sim$ 1 J (experiment 24) on the film causes coarsening and grain size growth, leading to an improved PF of 813.9  $\mu$ W m<sup>-1</sup> K<sup>-2</sup>

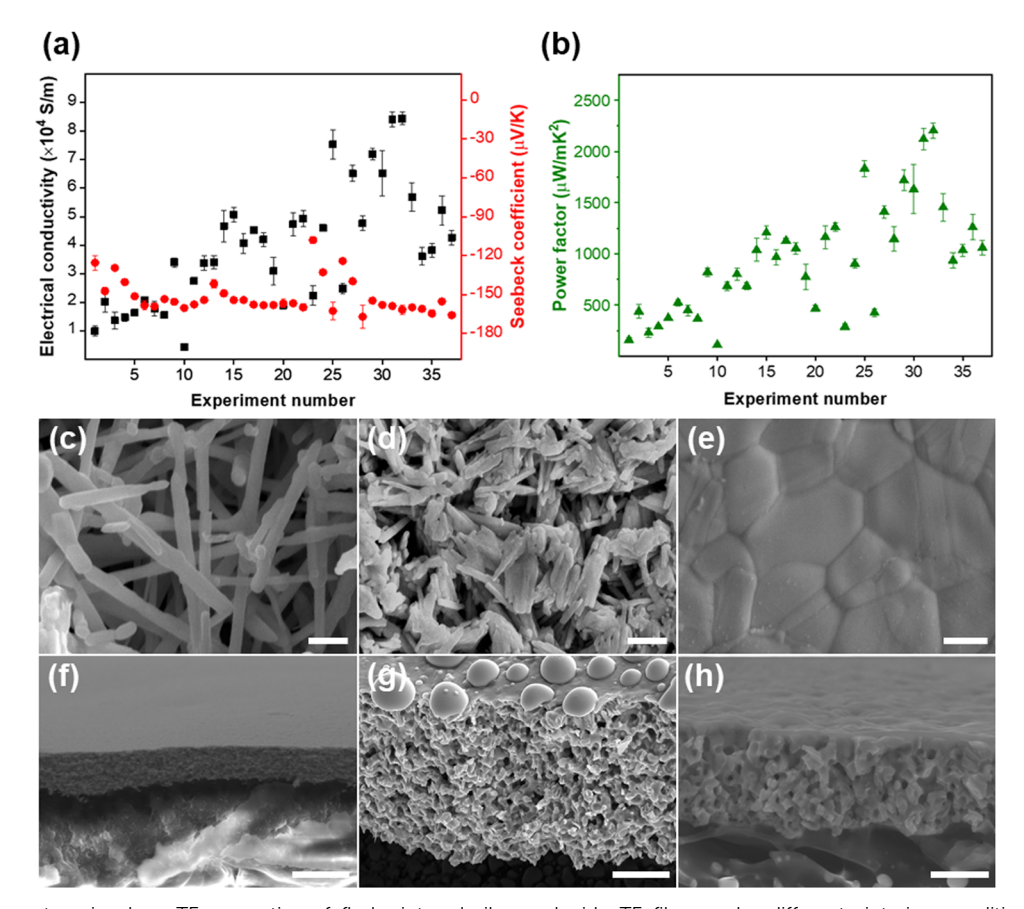


Fig. 2 Room-temperature in-plane TE properties of flash-sintered silver-selenide TE films under different sintering conditions (details of each experiment and sintering variables are summarized in Table S1, ESI†). (a) Electrical conductivity and the Seebeck coefficient. (b) Power factor. Surface SEM images showing the (c) unsintered silver-selenide film, (d) flash-sintered film under non-optimum sintering variables (experiment 24), and (e) flashsintered film under optimized sintering variables (experiment 32). Scale bars are 500 nm. Cross-sectional SEM images of the (f) unsintered film. Scale bar is 5 µm. (q) Film with 14.3 µm thickness (experiment 6). The scale bar is 5 µm. (h) Film with 2.3 µm thickness (experiment 28). The scale bar is 2 µm.

Table 1 Room-temperature TE properties of organic and inorganic TE materials including silver-selenide films with different compositions

Composition	Sintering time (s)	Seebeck coefficient (μV K <sup>-1</sup> )	Electrical conductivity (S m <sup>-1</sup> )	Thermal conductivity (W m <sup>-1</sup> K <sup>-1</sup> )	Power factor (μW m <sup>-1</sup> K <sup>-2</sup> )	zT	Ref.
Cu <sub>1</sub> Ag <sub>4</sub> Se <sub>3</sub>	1800	-45.7	$7.6 \times 10^{4}$	1.32	1594	0.4	11
PVP-Ag <sub>2</sub> Se	1800	-143.4	$9.3 \times 10^{4}$	0.51	1910	1.1	12
Ag <sub>2</sub> Se	1800	-143.0	$9.2 \times 10^4$	0.69	1882	0.8	13
Ag <sub>1.8</sub> Se	1800	-120.3	$6.7 \times 10^{4}$	NA	975 <sup>a</sup>	NA	17
Ag <sub>2</sub> Se/Se/polypyrrole	1800	-144.0	$10.6\times10^4$	0.71	2240	0.9	19
β-Ag <sub>2</sub> Se	1800	-140.7	$4.9 \times 10^4$	0.48	987	0.6	20
Sb <sub>1.6</sub> Bi <sub>0.4</sub> Te <sub>3</sub> /Te	2700	204	$7.2 \times 10^4$	0.9	3000	1	52
Sb <sub>2</sub> Te <sub>3</sub> /Te	3600	130	$7.8 \times 10^{4}$	NA	1370	NA	53
Te/PEDOT	600	115	$2.1 \times 10^4$	0.22	284	0.39	54
CNT/PANI	72 000	61	$6.1  imes 10^4$	0.7	220	0.1	55
Bi <sub>2</sub> Te <sub>3</sub>	600	-141	$6.7 \times 10^{4}$	1.2	1332	0.3	56
$Bi_{2}Te_{2.7}Se_{0.3}$	1.5	-163	$2.7 \times 10^{4}$	NA	730	NA	32
Ag <sub>1.96</sub> Se	<1	-161.7	$8.4 \times 10^4$	0.61	2205	1.1	This work
<sup>a</sup> Digitized from the refe	erence.						

(Fig. 2(d)). With optimized sintering variables and input energy (experiment 32), the grain size grows and porosity decreases, which results in the maximum PF and almost 22-fold enhancement compared to that of the unsintered film (Fig. 2(e)). It is

worth mentioning that the thickness of silver-selenide films in experiments 32 and 24 is 2.4 µm and 2.3 µm, respectively; however, the optimal input energy in experiment 32 is 6.9 J, which is almost 7-fold higher compared to that of experiment 24

(Table S1, ESI†). This highlights the impact of optimal sintering conditions on the TE properties. The corresponding TE properties in the SEM images are shown in Fig. S6 (ESI†).

Hall effect measurements were carried out to provide insight into the charge carrier transport behavior of the flash-sintered films. As shown in Table S3 (ESI $\dagger$ ), the carrier mobility  $\mu$  increases dramatically from 64.9 in unsintered films to 721.3 cm $^2$  V $^{-1}$  s $^{-1}$  in the sintered film under the optimized conditions (experiment 32). Here, the increased mobility can be ascribed to the increased film density and grain sizes with decreased grain boundaries, as shown in Fig. 2(e). The decreased carrier concentration in the sintered film explains the increase in the Seebeck coefficient after flash sintering. EDS analysis of sintered films under the optimized conditions revealed a slight shift in composition from Ag<sub>1.9</sub>Se (unsintered film) to Ag<sub>1.96</sub>Se (Table S4, ESI†). In addition, we conducted XRD analysis of silver-selenide films before and after flash sintering (experiment 32). The increase in X-ray diffraction intensity (Fig. S7, ESI†) indicates an improvement in crystallinity due to grain growth, which is consistent with the observation in SEM analysis. The unsintered sample shows weak characteristic peaks of (112) and (121) of silver-selenide and wide peaks near 16°-26°, of which the latter may correspond to the polymer substrate of the vacuum-filtrated films. The sintered film also exhibits an almost identical phase to the bulk silver-selenide crystal in the Inorganic Crystal Structure Database (ICSD#52603), indicating no obvious impurities.

In addition, we found that the thicknesses of silver-selenide films played an important role in the flash sintering process and the resulting TE properties. Fig. 2(f)-(h) shows crosssectional SEM images of unsintered and sintered films under the same input energy but with varying thicknesses. As shown in Fig. S8 (ESI†), sintering films under the same input energy of ~ 2.54 J (experiments 6 and 28) but with varying thicknesses of 14.3  $\mu$ m and 2.3  $\mu$ m result in PF values of 523.5  $\mu$ W m<sup>-1</sup> K<sup>-2</sup> and 1145.2 μW m<sup>-1</sup> K<sup>-2</sup>, respectively. The films with reduced thicknesses undergo more uniform heating and sintering across the entire thickness, thus possessing the potential to achieve a greater PF using the flash sintering [Fig. 2(g) and (h)]. Room-temperature TE properties (Fig. S8, ESI†) show a 128% enhancement of the electrical conductivity under the same input energy with reducing thickness. We observed that an excessive input energy on thin films could cause sublimation of the silver-selenide nanostructures and create disconnected and porous microstructures with very low PF (see Fig. S9, ESI†).

Among the optimized sintering variables, the pulse delay time between two adjacent pulses does not alter the input energy, but it impacts the microstructure and the resulting TE properties of the sintered films. Fig. S10 (ESI†) shows the room-temperature TE properties of the films under three sets of sintering variables with the same input energy for each set but different pulse delay times. We found that the PF increased with decreasing pulse delay time. For example, decreasing the pulse delay time from 1500 ms to 248 ms in experiments 13 and 15 (details in Table S1, ESI†), respectively, led to a 76.7% increase in PF. This is attributed to elevated temperatures because of the decreased pulse delay time between adjacent

pulses that leads to densified microstructures.<sup>51</sup> This phenomenon was also observed for the other TE material system (n-type Bi<sub>2</sub>Te<sub>2.7</sub>Se<sub>0.3</sub>) in our previous study.<sup>32</sup>

The thermal diffusivity of the silver–selenide film was measured using the Angstrom method, and the in-plane thermal conductivity  $\kappa$  was determined using the relationship  $\kappa = \alpha \rho c_{\rm p}$  where  $\alpha$ ,  $c_{\rm p}$ , and  $\rho$  are thermal diffusivity, specific heat capacity, and density, respectively. The in-plane  $\kappa$  of the silver–selenide films is 0.5 W m<sup>-1</sup> K<sup>-1</sup> before sintering. The in-plane  $\kappa$  increases to 0.61 W m<sup>-1</sup> K<sup>-1</sup> under the optimized sintering conditions (experiment 32), which leads to a zT value of 1.1 at room temperature. As shown in Fig. 2(h) and Fig. S11, and S12 (ESI†), the sintered film contains numerous pores of different sizes, which can effectively scatter phonons with short to long wavelengths and reduce lattice thermal conductivity. Details of the thermal conductivity measurement process are described in the Materials and methods section and the ESI.†

Fig. 3 demonstrates and explains the efficacy of the GPR machine learning model to predict the PF of the flash-sintered films as a function of four sintering variables (voltage, pulse duration, number of pulses, and pulse delay) and the thickness of the silver–selenide films.

The predicted power factors in Fig. 3(a) are generated iteratively (with constant hyperparameters) using data from the prior experiments. For example, the GPR prediction for experiment 7 uses data from the six prior experiments for training. Out of the five variables, the four sintering variables can be controlled by adjusting the flash sintering processing parameters, while the film thickness can be controlled by adjusting the silver-selenide particle concentration during the vacuum filtration process. Table S1 (ESI†) further divides the two groups of samples shown in Fig. 3(a) with average thicknesses of 2.6-12.5 µm into eight subgroups. Analysis of Fig. 3(a) and Table S1 (ESI†) shows that the GPR rapidly learns the process-property relationship and only needs one or two experiments in each thickness subgroup to make confident predictions on experiments with close distance (as explained in the Materials and methods section, each prediction is a "weighted sum" of prior experiments). For example, experiments 14-22 are in the 9 µm-thickness subgroup; experiment 14 has a high prediction uncertainty of  $\pm 545 \, \mu \text{W m}^{-1} \, \text{K}^{-2}$  as there are no prior experimental data for a sample with 9  $\mu m$ thickness. Experiment 15 has close distance with experiment 14; thus, after incorporating experiment 14 into the GPR model, the prediction uncertainty of experiment 15 reduced to  $\pm 192 \ \mu W \ m^{-1} \ K^{-2}$ . Experiment 16 is far away in distance compared with both experiment 14 and 15, leading to a high prediction uncertainty of  $\pm 508 \, \mu \text{W m}^{-1} \, \text{K}^{-2}$ ; on comparing experiment 16 with experiment 14, the prediction uncertainty decreased 6.7% because the prior experiments 14 and 15 enhance the confidence of the GPR model. As more data are added to each thickness subgroup near the optimal sintering conditions, one expects the GPR prediction uncertainty to converge to the experimental measurement uncertainty. In addition, Table S1 (ESI†) includes data for 8 experiments in which the thin film burned due to the excessive energy input, and the PF was

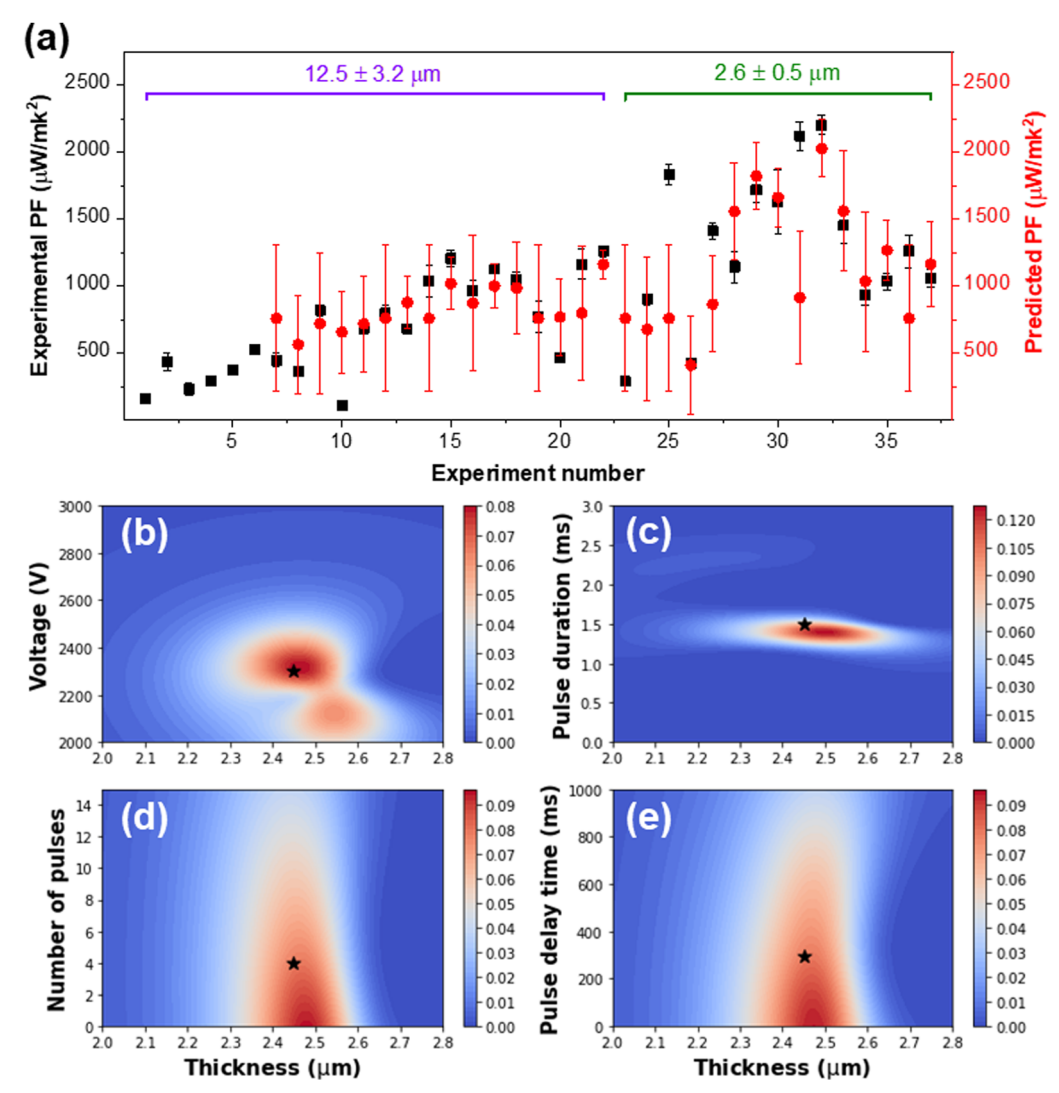


Fig. 3 (a) Comparison of the measured and machine learning-predicted power factors for sintered films. The red dots and error bars correspond to the GPR prediction mean and standard deviation. The black squares and error bars show the measured power factor. (b) – (e) Heatmaps show the sensitivity of the expected improvement (BO objective) as a function of thickness and (b) voltage, (c) pulse duration, (d) number of pulses, and (e) pulse delay time. The color scale from blue to red shows the expected improvement, where the red region indicates the range of optimal sintering variables. The black star marks the conditions of experiment 32 which had the maximum measured power factor.

measured to be zero. These experiments are not shown in Fig. 3(a) for clarity but were included in the GPR analysis. Inspecting the GPR hyperparameters,  $l_1 = 0.625$  (voltage),  $l_2 =$ 0.459 (pulse duration),  $l_3 = 5$  (number of pulses),  $l_4 = 2.36$  (pulse delay), and  $l_5$  = 0.0477 (thickness), reveals that the film thickness can influence effectiveness of the flash sintering process (as explained in the Materials and methods section, the importance of a feature is inversely proportional to its length scale l) and the thinner films typically have a higher PF compared to similar thicker films. As aforementioned, the films with reduced thicknesses experience more uniform heating and sintering across the entire thickness, leading to dense microstructures and a greater PF. These GPR results motivated the team to prepare the second group of thinner films shown in Fig. 3(a), which underscores the synergy between experiments and machine learning models. Fig. 3(b)-(e) shows the sensitivity of the expected

improvement metric (objective for BO) as a function of thickness and the other four flash sintering variables. Fig. S13 in the ESI† shows similar heatmaps for the prediction mean, prediction uncertainty, and expected improvement over a wider thickness range (1-16 μm). These heatmaps confirm that the GPR model predicts a narrow thickness range, 2.2-2.6 µm, which maximizes the expected improvement. Moreover, Fig. 3(b)-(e) and Fig. S13 (ESI†) show that voltage and pulse duration are important factors for the PF. Similarly, there is a wide range of pulse delay time and number of pulses that give a high expected improvement. This finding is consistent with the importance of features indicated by the length scales and the Pearson correlation matrix shown in Fig. S14 (ESI†). Furthermore, the gradual improvement in the PF in each thickness group emphasizes the importance of optimizing all flash sintering variables. In this application, the film thickness was determined by the vacuum filtration process.

The GPR model was then used to optimize the remaining four sintering variables with the thickness being held constant.

A key contribution of this work is the integration of BO recommendations and expert intuition to maximize the PF of flash-sintered silver-selenide TE films. To illustrate this integration, the results from experiments 23-30 in the second thickness group (2.6  $\pm$  0.5  $\mu$ m) were considered. Experiment 23 is chosen by intuition from previous experiments 1-22 as it is the first experiment in the 2.3 µm-thickness subgroup. The GPR was then updated to incoporate the result from experiment 23, and BO recommended up to five optimal conditions for the next experiment, which were then downselected by the experimental expert. Following this same procedure, the conditions for the next eight experiments (24-32) were chosen, resulting in a steady increase in the power factor. The maximum PF was achieved at experiment 32 (see details of sintering conditions in Table S1, ESI†), which is the final experiment in the sixth thickness subgroup (2.4 µm). We observed that the PF decreases for all subsequent five sintering experiments, which correspond to the seventh and eighth thickness subgroups (2.7 and 3.8 μm, respectively). One possibility, suggested in Fig. 3(b)-(e), is that there is a narrow range of thickness values, approximately 2.3-2.6 µm, for which the PF is maximized. The final five experiments (and two thickness subgroups) are outside this range.

Table 1 lists the room-temperature TE properties of several reported studies on organic and inorganic TE materials including flexible silver–selenide films fabricated using the vacuum-assisted filtration method. Our approach using machine learning for optimizing the flash sintering process not only results in an ultrahigh PF and zT, among the highest in n-type flexible TE materials, but also significantly decreases the sintering time to less than 1 second.

Apart from the TE properties, the flexibility and mechanical durability of the silver–selenide films play a vital role in fabricating flexible TEGs for practical applications (*e.g.*, wearable electronics). Fig. 4 demonstrates the average ratio of the electrical conductivity ( $\sigma/\sigma_0$ ), Seebeck coefficient ( $S/S_0$ ), and power

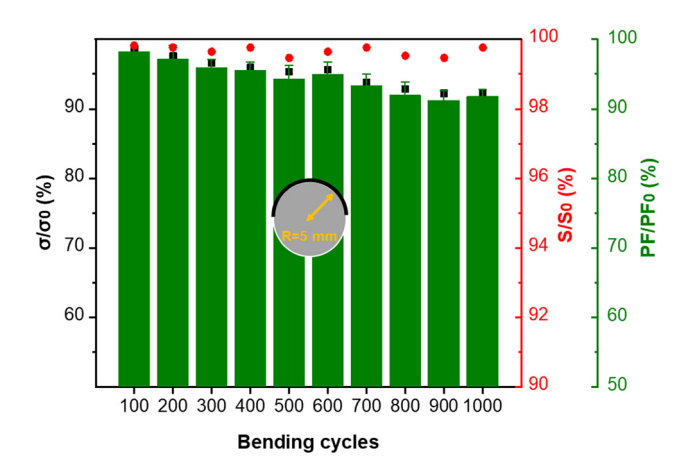


**Fig. 4** Flexibility test of the flash-sintered films. The electrical conductivity, the Seebeck coefficient, and the PF change of the films after bending for 1000 cycles. The bending radius is 5 mm.

factor (PF/PF<sub>0</sub>) as a function of bending cycles. Three samples were tested, and the error bar represents the standard deviation from these samples. We used a programmable linear motion slide for the bending test with a bending radius of 5 mm. Fig. S15 (ESI†) demonstrates the film at different bending angles. As shown in Fig. 4, the electrical conductivity decreases slightly with the increase in bending cycles whereas the Seebeck coefficient is almost stable. This leads to an about 8% decrease in the PF after 10³ bending cycles, which confirms the excellent flexibility and robustness of the sintered films. Table S5 (ESI†) lists flexibility of several recently reported studies on silverselenide films fabricated using the vacuum-assisted filtration method.

A flexible TEG was assembled with six silver-selenide legs sintered under the optimum conditions (experiment 32:2.3 kV voltage, 1.5 ms pulse duration, 4 pulses, and 293 ms pulse delay time) with an internal resistance of 75.8  $\Omega$ . Fig. S16 (ESI†) shows the fabricated TEG and the measurement setup. Details are included in the Materials and methods section. The theoretical internal resistance of the six silver-selenide legs is calculated to be 75.4  $\Omega$  using the resistivity and dimensions of the TE legs, which is in good agreement with the measured internal resistance. The small difference (<0.5%) between the measured and the theoretical resistances is attributed to the silver electrodes and the contact resistance between the TE legs and silver electrodes. Fig. 5(a) shows the measured device opencircuit voltage  $(V_{oc})$  under different temperature gradients up to 70 K. The measured values are almost equal to the theoretical values, which are calculated according to the expression  $V_{\rm oc}$  =  $N|S|\Delta T$ , where N is the number of TEG legs, S is the Seebeck coefficient, and  $\Delta T$  is the corresponding temperature gradient with the maximum output voltage of 67.5 mV at  $\Delta T$  of 70 K.

Fig. 5(b) shows the device operating voltage as a function of electrical current, where there is a linear negative correlation between the output voltage and the output current. Fig. 5(c) shows the device power output at different  $\Delta T$  values with the maximum power output of almost 16  $\mu$ W at  $\Delta T$  of 70 K. As conventionally calculated, 11,13,57 the power density can be obtained by dividing the generated power by the number of legs N and the cross-sectional area  $A = w \times t$ , where w is the width of films and t is the thickness of silver-selenide films. As shown in Fig. 5(d), the maximum power density is calculated to be 0.5 and 26.6 mW cm<sup>-2</sup> at  $\Delta T$  of 10 and 70 K, respectively. This is sufficient to power a variety of low-energy consumption Internet of Things sensors. In addition, we demonstrated a wearable TEG to harvest heat from the human body and convert it to electricity. Fig. 6 shows the flexible TEG with an internal resistance of 56  $\Omega$ , which was tied around an arm with a generated voltage of 1.4 mV at  $\Delta T$  of  $\sim$  1.8 K between the hot side and the cold side of the device.

We also tested the stability of the TEG by exposing it to the air for a month and monitored the internal resistance change over time. After being exposed to air, the internal resistance of the device increased by  $\sim 0.5\%$  to  $76.2~\Omega$ , showing an excellent stability of the sintered silver–selenide films even without encapsulation. The flexible TEG can be applied to harvest energy from other heat sources with higher temperatures than

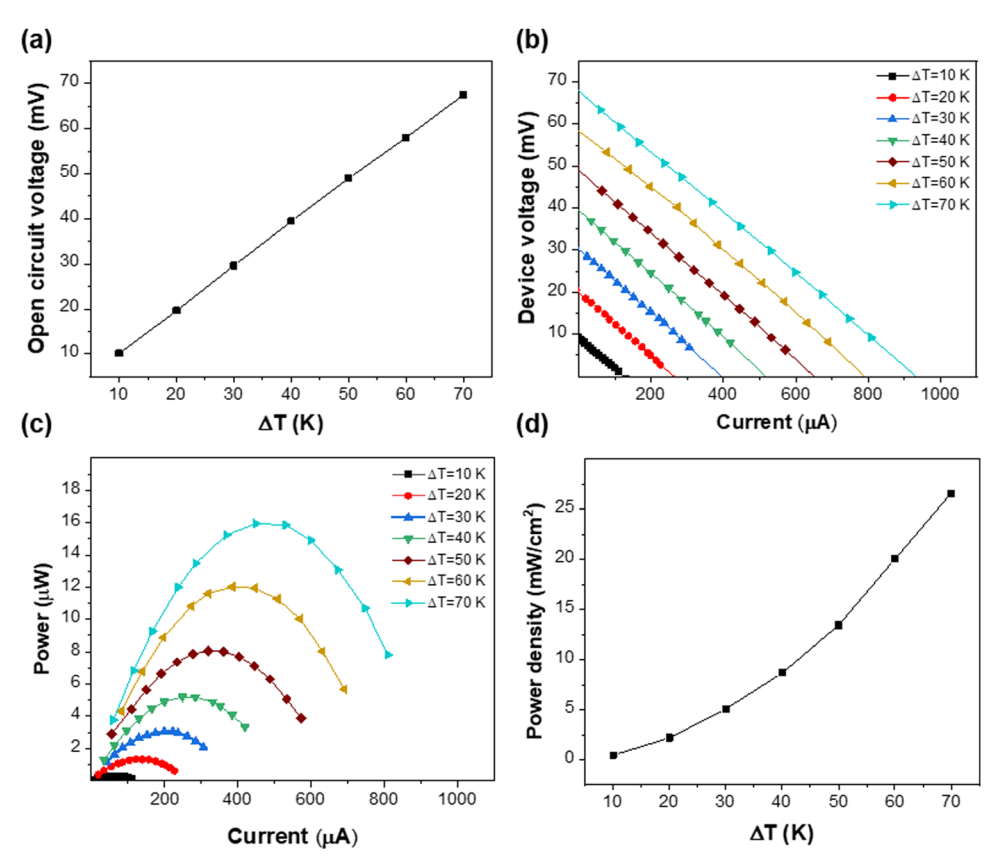


Fig. 5 Performance of a flexible TEG fabricated using flash-sintered silver-selenide films. (a) Open-circuit voltage at different temperature gradients. (b) Device operating voltage versus current at various  $\Delta T$  values. (c) Power output versus electrical current. (d) Electrical power density at various  $\Delta T$  values.

the human body, such as power plants, factories, industrial machines, geothermal and other low-grade waste heat sources. In addition to energy harvesting, an alternative application could be thermoelectric coolers (TECs) based on the Peltier effect. TECs have exhibited significant advantages compared to conventional vapor-compression refrigeration systems, including small size, free of noise, moving parts, working fluid, and chemical reaction.<sup>58,59</sup>

As demonstrated by these results, this study highlights the synergies between machine learning-enabled Bayesian optimization and expert-driven experimental search. Human intuition is critical to defining the BO problem by identifying the experimental decision variables and their bounds. GPR is especially well-suited for sparse noisy data arising from expensive experiments as GPR "intelligently interpolates" from prior experiments. Early in the experimental campaign, we purposefully explored a

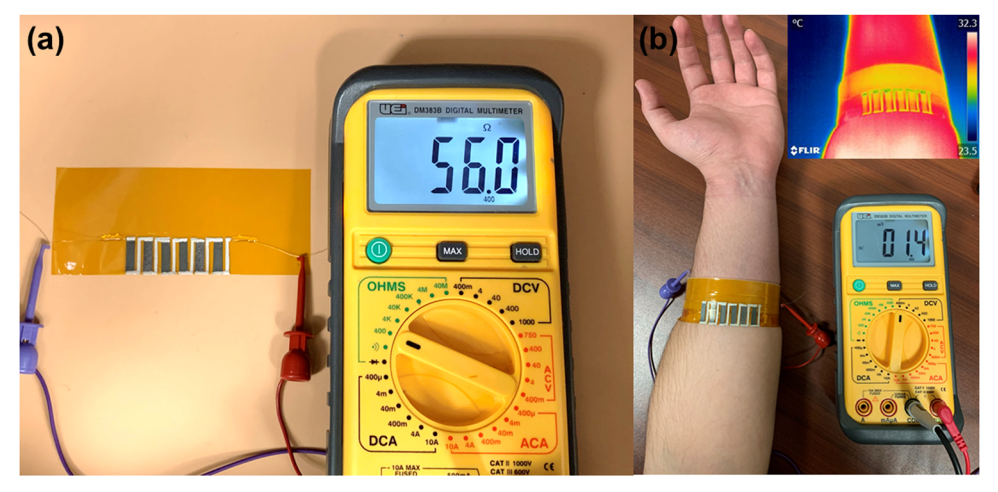


Fig. 6 Performance of a wearable TEG. (a) Internal resistance of the TEG fabricated using six silver–selenide films. (b) Digital photograph of 1.4 mV opencircuit voltage generated at a  $\Delta T$  of  $\sim 1.8$  K between the hot side and the cold side of the device. The inset is the corresponding infrared thermal image.

mix of BO and human-recommended sintering conditions. The latter helped bias the search to consider unexplored regions of the decision space based on prior knowledge. Later in the campaign, we used expert intuition to downselect the recommended experimental conditions with similar EI scores. We found these strategies to be less cumbersome than designing custom GPR kernels to incorporate the said prior knowledge. 40,60 Moreover, this study demonstrates the robustness and flexibility of the GPR strategy as we successfully extended the GPR input space to include thickness partway through the experimental campaign. Although GPR models do not offer full mechanistic insights, analysis of the kernel length scales provides a relative importance of each input variable. We used this information to design one-dimensional sensitivity analyses under the optimal sintering conditions and perform the corresponding material characterization to develop a mechanistic understanding of the results (Fig. 2 and Fig. S5, S7, S11, and S12, Tables S2-S4, ESI†). Moreover, emerging physics-based machine learning models can be incorporated into the proposed framework. In our opinion, these synergies between machine learning and expert intuition are key factors to success.

# 3. Conclusions

In summary, we report the first machine learning-assisted ultrafast flash sintering of flexible silver-selenide TE devices for energy harvesting applications. BO significantly accelerated our findings of a set of intense pulsed light (flash) sintering variables, leading to an ultrahigh power factor of 2205  $\mu W~m^{-1}~K^{-2}$  and a zT of 1.1 at room temperature realized with a sintering time less than 1.0 second. Flash-sintered films demonstrate outstanding flexibility with 92% retention of the PF after 10<sup>3</sup> bending cycles. The maximum power density of a six-leg TEG is 0.5 and 26.6 mW cm<sup>-2</sup> at  $\Delta T$  of 10 K and 70 K, respectively. The ultrahigh-performance, low-cost, and highly flexible silverselenide TE films show great potential for energy harvesting and wearable devices. Although this study focuses on the optimization of flash sintering for silver-selenide TE materials, this machine learning-assisted experimentation strategy possesses the potential for ultrafast sintering of other TE material systems (e.g., Bi<sub>2</sub>Te<sub>3</sub> and Sb<sub>2</sub>Te<sub>3</sub>) and roll-to-roll manufacturing of a broad range of energy, thermal, and electronic devices.

#### 4. Materials and methods

#### Synthesis of silver-selenide nanostructures

The silver–selenide nanostructures were prepared by a bottom-up synthesis approach. Selenium dioxide (2.5 g) and polyvinylpyrrolidone (PVP, 0.05 g) are dissolved in 200 mL of deionized water, followed by the addition of 60 mL of ethanol to adjust the surface tension of the solution. The above solution was then added dropwise to a stirred solution of ascorbic acid (3.2 wt%, 200 mL) in water, leading to the formation of selenium nanowires (red). After vigorously stirring for 1 h, a stoichiometric amount of silver precursor solution (AgNO<sub>3</sub> in water) was introduced to the

above mixture and left to react overnight. The final product was collected by centrifugation and then washed with water and ethanol each three times before use.

#### Characterization

Crystal structures of the synthesized nanostructures were examined via X-ray diffractometry (XRD; MiniFlex; Rigaku) using Cu Ka radiations over a  $2\theta$  range of 20–60. Microstructures and chemical compositions of the TE films were examined using a scanning electron microscope (Helios G4 Ux Dual Beam) coupled with an energy-dispersive X-ray spectrometer (Bruker).

#### Flash sintering of silver-selenide films

Flash sintering was performed using a Sinteron 2100 system (Xenon Corp., USA) with a 107 mm xenon spiral lamp. The S-2100 system was configured for maximum pulse durations of 3 ms with the sintering carried out in an ambient environment. The S-2100 produced the pulse energy (single) ranging from 30 to 2850 J.

The room-temperature Seebeck coefficient and electrical conductivity are measured using a custom-built setup. We used

#### Measurement of TE properties

the four-point probe method for electrical conductivity measurement. To measure the thickness of the films precisely, we used cryogenic cooling of the films by liquid nitrogen to create sharp edges for measuring the thickness using SEM, as shown in Fig. S5 (ESI†). For Seebeck coefficient measurement, we applied a temperature gradient (6 K) across the film and measured the induced voltage and temperatures using k-type thermocouples. The Seebeck coefficient is calculated as  $S = \frac{-\Delta V}{\Delta T}.$  The measurement error of the custom-built apparatus was  $\sim$  5% for both the electrical conductivity and Seebeck coefficient. Details of the measurements are described in our previous work.61 We used the Angstrom method for in-plane thermal conductivity measurement of the silver-selenide films. The room-temperature in-plane thermal conductivity  $\kappa$  was determined by measuring the thermal diffusivity  $\alpha$ , specific heat capacity  $c_p$ , and density  $\rho$ , using the relationship  $\kappa = \alpha \rho c_p$ . Thermal diffusivity was measured using the Angstrom method by applying a sinusoidal heat signal at one end of the sample and measuring the temperature response as a function of time at two different locations along with the sample. Fig. S12 (ESI†) shows the cross-sectional SEM image of the film used for thermal diffusivity measurement. The thermal diffusivities of both the porous filtration membrane and the combined membrane and silver-selenide films are measured. Modified effective medium theory was used to extract the thermal conductivity of the silverselenide film itself. Details of the measurement process and thermal conductivity extraction are described in the ESI.† The thermal conductivity measurement error was estimated to be

around 10%. Specific heat capacity and density values are adopted

from a previous report.<sup>57</sup>

#### Hall effect measurement

The Hall effect measurement is conducted to measure the room-temperature carrier transport properties of unsintered and flash-sintered silver-selenide films under the optimized conditions (experiment 32). Table S3 (ESI†) shows the carrier mobility  $(\mu)$  and carrier concentration (n). We used an automatic Hall effect measurement system (INSTEC, H8200) for room-temperature carrier mobility and concentration measurement. We measured two films (10 mm × 10 mm) for each condition (unsintered and sintered). To minimize the electrical contact resistance between the leads and the film, four corners of the film (100  $\mu$ m  $\times$  100  $\mu$ m) were sputter-coated with a 30 nm layer of 80% Au and 20% Pd.

#### TEG fabrication and testing

Two thermoelectric generators were assembled with six silverselenide films sintered under the optimum conditions (experiment 32:2.3 kV voltage, 1.5 ms pulse duration, 4 pulses, and 293 ms pulse delay) on mica and flexible polyimide substrates with 150 µm and 25  $\mu m$  thickness, respectively. Each leg with a size of 12 mm imes4 mm  $\times$  2.5  $\mu$ m was attached to the substrate using double-sided tape. To minimize the contact resistance, both ends of each film (1 mm × 4 mm) were sputter-coated with a 30 nm layer of 80% Au and 20% Pd and then the legs were connected by silver paste (Flash-dry, SPI). We used a custom-built in-house apparatus for measuring the device performance under different temperature gradients with two k-type thermocouples for measuring cold- and hot-side temperatures as shown in Fig. S16 (ESI†).

#### Design of initial experiments

Special care is required to select the initial training data used for machine learning-based optimization of experiments.<sup>62</sup> In this work, to determine the parameters for experiments 1 to 6 in Table S1 (ESI†), we consider two factors for three sintering variables: voltage (2.2 or 2.4 kV), pulse duration (1 or 2 ms) and number of pluses (1 pulse or 5 pulses with 1000 ms pulse delay). Thickness was held constant. Instead of performing a full factorial design  $(2^3 = 8)$ , we decided to omit the two experiments with 2 ms pulse duration and 5 pulses to avoid burning any samples (based on our prior experience). The data from these first six experiments were used for training the initial machine learning models.

#### Machine learning and Bayesian optimization

Gaussian Process Regression (GPR) and Bayesian Optimization (BO) are popular machine learning techniques to intelligently improve expensive experiments through adaptive learning. In this section, we describe the underlying mathematics behind GPR and BO and emphasize specific details for implementation with TE materials.

Let f(x) represent an unknown function that maps experiment conditions x (input, vector) and power factor y (output, scalar). Mathematically, we seek to solve the optimization problem  $\max_{x \in X} f(x)$ , where the set x contains all possible (feasible) experimental conditions. However, experiments are expensive

and time-consuming. BO recommends a sequence of experiments to maximize the power factor using three main steps: first the GPR machine learning model is trained on the available data to emulate the unknown function f(x). Second, decision theory is used to recommend the most valuable experiments; third, the proposed experiments are conducted, measured, and recorded. The process is repeated multiple times until the desired power factor is obtained or the experimental budget is exhausted.

A single flash sintering experiment requires specifying five input variables – voltage  $(x_{i1})$ , pulse duration  $(x_{i2})$ , pulse delay  $(x_{i3})$ , number of pulses  $(x_{i4})$ , and thickness  $(x_{i5})$  – which result in a corresponding power factor  $(y_i)$ . Here the subscript i denotes the experiment (sample) number. All samples are combined for the data set  $D = \{(\mathbf{x}_i, \mathbf{y}_i), | \mathbf{x}_i \in \mathbb{R}^5, \mathbf{y}_i \in \mathbb{R}, i \in 1,...,N\}$ , abbreviated as D = (X, y).

We now construct a GPR model to predict the outcome of a new experiment,  $f(x_*)$ , under conditions  $x_*$ . GPR is a nonparametric model, which means that the data D are directly embedded into the model. The GPR model is fully specified using the data set D, the mean function m(x), and the kernel (covariance) function K(X, X') In this work, we use the radial

basis function as the kernel  $k_{\text{RBF}}(x, x'|I) = e^{-\frac{1}{2}\sum_{j=1}^{5} \left(\frac{x_j - x_j'}{I_j}\right)^2}$ , which measures the distance between each pair of experimental conditions x and x'. Thus, when making a prediction under a new experimental condition  $x_*$ , the GPR incorporates all information from data set D using the kernel to "weight" the importance of all prior experiments using the distance between  $x_*$  and all  $x_i \in D$ . In this way, the GPR is a sophisticated ML approach to interpolate between all prior experiments in D without requiring an assumed parametric model to map inputs  $x_i$  to output y. Instead, the GPR model assumes the experimental outcomes are described by a multivariate normal distribution N(...):

$$\begin{bmatrix} f(X) \\ f(x_*) \end{bmatrix} \sim N \left( \begin{bmatrix} m(X) \\ m(x_*) \end{bmatrix}, \begin{bmatrix} K(X,X) & K(X,x_*) \\ K(x_*,X) & k(x_*,x_*) \end{bmatrix} \right)$$
(1)

Applying Bayes rule of probability gives the following analytical expressions for predicting mean and variance under the new experimental condition  $x_*$ :<sup>63</sup>

$$\mu_*(\mathbf{x}_*) = E(f(\mathbf{x}_*)|\mathbf{y}) = \mathbf{m}(\mathbf{x}_*) + \mathbf{K}(\mathbf{x}_*, \mathbf{X})[\mathbf{K}(\mathbf{X}, \mathbf{X}) + \sigma^2 \mathbf{I}]^{-1} (\mathbf{y} - \mathbf{m}(\mathbf{X}))$$
(2a)

$$\sigma_*(\mathbf{x}_*) = \operatorname{Var}(f(\mathbf{x}_*)|\mathbf{y}) = k(\mathbf{x}_*, \mathbf{x}_*) - K(\mathbf{x}_*, \mathbf{X})[K(\mathbf{X}, \mathbf{X}) + \sigma^2 \mathbf{I}]^{-1} K(\mathbf{X}, \mathbf{x}_*))$$
(2b)

Eqn (2) also includes normally distributed observation errors  $l_3$ ,  $l_4$ ,  $l_5$ )<sup>T</sup> in the kernel function  $k_{RBF}(\mathbf{x}, \mathbf{x}')$ , also called length scales, determine the importance of the features. If length scale  $l_i$  is small, then the corresponding feature  $x_i$  is more important to predict the output y. Optimal length scales are computed by maximizing log marginal likelihood (LML).<sup>60,64</sup>

Expected Improvement (EI) in a popular acquisition function is used to recommend an optimal  $x_*$  in a BO framework.

EI balances the trade-offs between exploration, *i.e.*, choosing x-in regions with high uncertainty and exploitation, *i.e.*, choosing x- in regions that will maximize f(x). EI achieves this balance by computing the expected value of the improvement between f(x) and f(x), where x is the experimental condition in data set D that has the highest power factor. Thus mathematically EI(x) = E[max(f(x) - f(x), 0)]. By exploiting mathematical properties of the normal distribution, EI(x) has the following analytical formula:

$$\mathrm{EI}(\mathbf{x}_*) = \begin{cases} (\mu_*(\mathbf{x}_*) - f(\mathbf{x}^+)) \varPhi(z(\mathbf{x}_*)) + \sigma_*(\mathbf{x}_*) \varphi(z(\mathbf{x}_*)), & \sigma_*(\mathbf{x}_*) > 0 \\ 0, & \text{otherwise} \end{cases}$$

$$z(\mathbf{x}_*) = \begin{cases} \frac{(\mu_*(\mathbf{x}_*) - f(\mathbf{x}^+))}{\sigma_*(\mathbf{x}_*)}, & \sigma_*(\mathbf{x}_*) > 0\\ 0, & \text{otherwise} \end{cases}$$
(3b)

Here,  $\Phi(\cdot)$  is the cumulative distribution function, and  $\phi(\cdot)$  is the probability density function, respectively, for the standard normal distribution. The GPR and BO workflows were implemented in Scikit learn.<sup>65</sup> The entire workflow, including the interaction between BO and human experts (experimentalist), is illustrated in Fig. 7. The entire procedure including hypertuning training and EI optimization requires less than 2 minutes on a MacBook with a 2.6 GHz Intel Core i7 CPU.

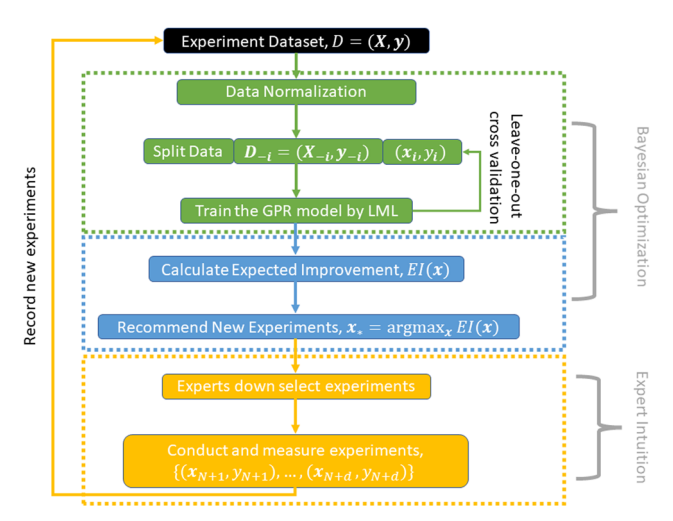


Fig. 7 The proposed workflow integrates Bayesian optimization (BO) and human intuition. The overall procedure contains three steps: Gaussian process regression (GPR) model training (green box), expected improvement (EI) calculation (blue box), and experimentalist downselection and fabrication (yellow box). The BO is implemented in first two steps, and expert intuition is incorporated in the last one. The data set, D = (X, y), contains N samples of recorded sintering variables  $\textbf{x}_i$ , which consist of voltage  $(x_{i3})$ , pulse duration  $(x_{i2})$ , pulse delay  $(x_{i3})$ , number of pulses  $(x_{i4})$ , and thickness  $(x_{i5})$ , and the corresponding power factor  $(y_i)$ . In each iteration, data set D is provided to BO, and d new experiments,  $\{(x_{N+1},y_{N+1}),...,(x_{N+d},y_{N+d})\}$ , are selected by human intuition, performed, and added to data set D; the procedure terminates when the expected improvement approaches zero or the experimental budget is exhausted.

### Conflicts of interest

There are no conflicts to declare.

# Acknowledgements

We would like to acknowledge support from the U.S. Department of Energy under awards DE-EE0009103. Y. Z. would like to acknowledge funding support from the National Science Foundation under award CMMI-1747685 and the U.S. Department of Energy under award DE-NE0008812.

# References

- J. Liang, T. Wang, P. Qiu, S. Yang, C. Ming, H. Chen,
   Q. Song, K. Zhao, T.-R. Wei, D. Ren, Y.-Y. Sun, X. Shi,
   J. He and L. Chen, *Energy Environ. Sci.*, 2019, 12, 2983–2990.
- 2 B. Lee, H. Cho, K. T. Park, J.-S. Kim, M. Park, H. Kim, Y. Hong and S. Chung, *Nat. Commun.*, 2020, **11**, 5948.
- 3 A. Nozariasbmarz, H. Collins, K. Dsouza, M. H. Polash, M. Hosseini, M. Hyland, J. Liu, A. Malhotra, F. M. Ortiz, F. Mohaddes, V. P. Ramesh, Y. Sargolzaeiaval, N. Snouwaert, M. C. Özturk and D. Vashaee, *Appl. Energy*, 2020, 258, 114069.
- 4 M. Dargusch, W. D. Liu and Z. G. Chen, Adv. Sci., 2020, 7, 2001362.
- 5 S. Masoumi, S. O. Shaughnessy and A. Pakdel, *Nano Energy*, 2022, **92**, 106774.
- 6 G. J. Snyder and E. S. Toberer, Nat. Mater., 2008, 7, 105-114.
- 7 M. He, F. Qiu and Z. Lin, Energy Environ. Sci., 2013, 6, 1352.
- 8 Y. Du, S. Z. Shen, K. Cai and P. S. Casey, *Prog. Polym. Sci.*, 2012, **37**, 820–841.
- 9 H. Goldsmid, Materials, 2014, 7, 2577-2592.
- 10 I. T. Witting, T. C. Chasapis, F. Ricci, M. Peters, N. A. Heinz, G. Hautier and G. J. Snyder, Adv. Electron. Mater., 2019, 5, 1800904.
- 11 Y. Lu, Y. Qiu, K. Cai, Y. Ding, M. Wang, C. Jiang, Q. Yao, C. Huang, L. Chen and J. He, *Energy Environ. Sci.*, 2020, 13, 1240–1249.
- 12 C. Jiang, P. Wei, Y. Ding, K. Cai, L. Tong, Q. Gao, Y. Lu, W. Zhao and S. Chen, *Nano Energy*, 2021, **80**, 105488.
- 13 C. Jiang, Y. Ding, K. Cai, L. Tong, Y. Lu, W. Zhao and P. Wei, *ACS Appl. Mater. Interfaces*, 2020, **12**, 9646–9655.
- 14 P. Jood, R. Chetty and M. Ohta, *J. Mater. Chem. A*, 2020, **8**, 13024–13037.
- 15 S. Jo, S. Cho, U. J. Yang, G. S. Hwang, S. Baek, S. H. Kim, S. H. Heo, J. Y. Kim, M. K. Choi and J. S. Son, *Adv. Mater.*, 2021, 33, 2100066.
- 16 J. A. Perez-Taborda, O. Caballero-Calero, L. Vera-Londono, F. Briones and M. Martin-Gonzalez, Adv. Energy Mater., 2017, 8, 1702024.
- 17 Q. Gao, W. Wang, Y. Lu, K. Cai, Y. Li, Z. Wang, M. Wu, C. Huang and J. He, ACS Appl. Mater. Interfaces, 2021, 13, 14327–14333.
- 18 S. Hou, Y. Liu, L. Yin, C. Chen, Z. Wu, J. Wang, Y. Luo, W. Xue, X. Liu, Q. Zhang and F. Cao, *Nano Energy*, 2021, 87, 106223.

- 19 Y. Li, Q. Lou, J. Yang, K. Cai, Y. Liu, Y. Lu, Y. Qiu, Y. Lu, Z. Wang, M. Wu, J. He and S. Shen, Adv. Funct. Mater., 2021, 32, 2106902.
- 20 Y. Ding, Y. Qiu, K. Cai, Q. Yao, S. Chen, L. Chen and J. He, Nat. Commun., 2019, 10, 841.
- 21 M. Oghbaei and O. Mirzaee, J. Alloys Compd., 2010, 494, 175-189.
- 22 L. Shi, M. Layani, X. Cai, H. Zhao, S. Magdassi and M. Lan, Sens. Actuators, B, 2018, 256, 938-945.
- 23 J. Xi, K. Xi, A. Sadhanala, K. H. L. Zhang, G. Li, H. Dong, T. Lei, F. Yuan, C. Ran, B. Jiao, P. R. Coxon, C. J. Harris, X. Hou, R. V. Kumar and Z. Wu, Nano Energy, 2019, 56, 741-750.
- 24 D. Dudina, B. Bokhonov and E. Olevsky, Materials, 2019, 12, 541.
- 25 R. R. Mishra and A. K. Sharma, Composites, Part A, 2016, 81, 78-97.
- 26 W. Mi, P. Qiu, T. Zhang, Y. Lv, X. Shi and L. Chen, Appl. Phys. Lett., 2014, 104, 133903.
- 27 T. Mineta, T. Saito, T. Yoshihara and H. Sato, Mater. Sci. Eng., A, 2019, 754, 258-264.
- 28 E. B. Secor, T. Z. Gao, M. H. Dos Santos, S. G. Wallace, K. W. Putz and M. C. Hersam, ACS Appl. Mater. Interfaces, 2017, 9, 29418-29423.
- 29 Y. Galagan, E. W. C. Coenen, R. Abbel, T. J. van Lammeren, S. Sabik, M. Barink, E. R. Meinders, R. Andriessen and P. W. M. Blom, Org. Electron., 2013, 14, 38-46.
- 30 M. Hösel and F. C. Krebs, J. Mater. Chem., 2012, 22, 15683.
- 31 S. Norita, D. Kumaki, Y. Kobayashi, T. Sato, K. Fukuda and S. Tokito, Org. Electron., 2015, 25, 131-134.
- 32 M. Saeidi-Javash, W. Kuang, C. Dun and Y. Zhang, Adv. Funct. Mater., 2019, 29, 1901930.
- 33 T. Wang, C. Zhang, H. Snoussi and G. Zhang, Adv. Funct. Mater., 2019, 30, 1906041.
- 34 Z. Hou, Y. Takagiwa, Y. Shinohara, Y. Xu and K. Tsuda, ACS Appl. Mater. Interfaces, 2019, 11, 11545-11554.
- 35 Y. Iwasaki, I. Takeuchi, V. Stanev, A. G. Kusne, M. Ishida, A. Kirihara, K. Ihara, R. Sawada, K. Terashima, H. Someya, K.-ichi Uchida, E. Saitoh and S. Yorozu, Sci. Rep., 2019, 9(1), 2751.
- 36 C. Tian, T. Li, J. Bustillos, S. Bhattacharya, T. Turnham, J. Yeo and A. Moridi, Adv. Intell. Syst., 2021, 3, 2100014.
- 37 C. Wang, X. P. Tan, S. B. Tor and C. S. Lim, Addit. Manuf., 2020, 36, 101538.
- 38 T. Erps, M. Foshey, M. K. Luković, W. Shou, H. H. Goetzke, H. Dietsch, K. Stoll, B. von Vacano and W. Matusik, Sci. Adv., 2021, 7, eabf7435.
- 39 R.-R. Griffiths and J. M. Hernández-Lobato, Chem. Sci., 2020, 11, 577-586.
- 40 K. Wang and A. W. Dowling, Curr. Opin. Chem. Eng., 2022, 36, 100728.
- 41 U. Erturun, K. Erermis and K. Mossi, Appl. Energy, 2015, 159,
- 42 A. Kumar, K. Singh and R. Das, Appl. Therm. Eng., 2019, 159, 113935.

- 43 A. Kanatzia, C. Papageorgiou, C. Lioutas and T. Kyratsi, J. Electron. Mater., 2012, 42, 1652-1660.
- 44 R. B. Gramacy, Surrogates: Gaussian process modeling, design, and optimization for the Applied Sciences, CRC Press, Taylor & Francis Group, Boca Raton, FL, 2020.
- 45 J. Recatala-Gomez, A. Suwardi, I. Nandhakumar, A. Abutaha and K. Hippalgaonkar, ACS Appl. Energy Mater., 2020, 3, 2240-2257.
- 46 C. Zeng, W. Zhang, S. Ding, Z. Yang, H. Zeng and Z. Li, CrystEngComm, 2013, 15, 5127.
- 47 P. Jood, R. Chetty and M. Ohta, J. Mater. Chem. A, 2020, 8, 13024-13037.
- 48 C. Lee, Y.-H. Park and H. Hashimoto, J. Appl. Phys., 2007, **101**, 024920.
- 49 F. F. Aliev, M. B. Jafarov and V. I. Eminova, Semiconductors, 2009, 43, 977-979.
- 50 M. Ferhat and J. Nagao, J. Appl. Phys., 2000, 88, 813-816.
- 51 L. Ward, A. Agrawal, A. Choudhary and C. Wolverton, npj Comput. Mater., 2016, 2, 16028.
- 52 T. Varghese, C. Dun, N. Kempf, M. Saeidi-Javash, C. Karthik, J. Richardson, C. Hollar, D. Estrada and Y. Zhang, Adv. Funct. Mater., 2019, 30, 1905796.
- 53 C. Dun, W. Kuang, N. Kempf, M. Saeidi-Javash, D. J. Singh and Y. Zhang, Adv. Sci., 2019, 6, 1901788.
- 54 E. Jin Bae, Y. Hun Kang, K.-S. Jang and S. Yun Cho, Sci. Rep., 2016, 6, 18805.
- 55 H. Wang, S. Yi, X. Pu and C. Yu, ACS Appl. Mater. Interfaces, 2015, 7, 9589-9597.
- 56 S. J. Kim, J. H. We and B. J. Cho, Energy Environ. Sci., 2014, 7, 1959.
- 57 J. Gao, L. Miao, H. Lai, S. Zhu, Y. Peng, X. Wang, K. Koumoto and H. Cai, iScience, 2020, 23, 100753.
- 58 W. Y. Chen, X. L. Shi, J. Zou and Z. G. Chen, Small Methods, 2022, 6, 2101235.
- 59 S. H. Zaferani, M. W. Sams, R. Ghomashchi and Z.-G. Chen, Nano Energy, 2021, 90, 106572.
- 60 C. M. Bishop, Pattern recognition and machine learning, Springer New York, New York, NY, 2016.
- 61 M. Zeng, H. Xie, M. Saeidi-Javash, A. N. M. Tanvir, Y. Du, J. Chen, M. G. Kanatzidis and Y. Zhang, J. Mater. Chem. A, 2021, 9, 22555-22562.
- 62 B. Cao, L. A. Adutwum, A. O. Oliynyk, E. J. Luber, B. C. Olsen, A. Mar and J. M. Buriak, ACS Nano, 2018, 12, 7434-7444.
- 63 A. Günter, R. Kruse and B. Neuman, in Ki 2003: Advances in artificial intelligence: 26th annual German conference on AI, ki 2003, Hamburg, Germany, September 15-18, 2003: Proceedings, Springer, Berlin, 2003.
- 64 K. Wang, M. Saeidi-Javash, M. Zeng, Z. Liu, Y. Zhang, T. Luo and A. W. Dowling, Comput.-Aided Chem. Eng., 2022, 1819-1824.
- 65 F. Pedregosa, G. Varoquaux, A. Gramfort, V. Michel, B. Thirion, O. Grisel, M. Blondel, P. Prettenhofer, R. Weiss, V. Dubourg, J. Vanderplas, A. Passos, D. Cournapeau, M. Brucher, M. Brucher and E. Duchesnay, J. Mach. Learn. Res., 2011, 12, 2825-2830.